Chapter II.7
Validation of Satellite Rain Rate Estimation with Ground-Based Observing Systems

P. Antonelli, S. Puca, F. Zauli, R. Bennartz, L. de Leonibus, W. Feltz, and H. Woolf

1 Introduction

The goal of the described work is to present an experimental product for the estimation of convective precipitation rain rates (RR) from satellite observations and the procedure used to create and evaluate the new product. The algorithm, developed to estimate convective RR, combines an existing precipitation product based on AMSU data and developed under the Nowcasting Satellite Application Facility (SAF) (Bennartz 2005) with a convection detection algorithm based on SEVIRI data and developed at the Italian Centro Nazionale di Meteorologia e Climatologia Aeronautica (CNMCA). The convective precipitation derived by the combination of these two products is intended to be used by hydrologists for civil protection purposes. The described validation procedure was not only relevant to the overall product accuracy evaluation, but also represented a critical component for the development of the merging algorithm. The chapter is divided into sections which describe:

- the available in situ data and their consistency;
- the precipitation product from AMSU (theoretical basis for precipitation algorithm, product description, product validation and consequent error characterization, and algorithm improvements);
- the convection detection algorithm based on SEVIRI data (theoretical basis for the convection detection algorithm, product validation and consequent error characterization, and algorithm improvements);
- the convective precipitation product based on the merging of precipitation (AMSU) and convection (SEVIRI) products (methodology, product description, and product validation);
- the conclusions on:
  - validation issues related to the scientific hypothesis behind the merging algorithm;

P. Antonelli (✉)
CIMSS/University of Wisconsin, Madison, WI, USA
e-mail: paoloa@ssec.wisc.edu

D. Cimini et al. (eds.), *Integrated Ground-Based Observing Systems*,
DOI 10.1007/978-3-642-12968-1_14,

- the individual modules used to derive the convective precipitation product;
- the accuracy of available observations;
- the accuracy of the final derived product.

2 Available in Situ Data

This section describes the in situ observations used to develop and evaluate the convective precipitation product (RADAR RR and rain gauge values) and presents a qualitative comparison between them.

2.1 RADAR

The Italian Department of Civil Protection (DPC), through the network of the Regional Functional Centers, collects in real and near real-time RADAR data for the hydro-meteorological monitoring and management. Using these observations, the Meteorological Service of the Air Force (CNMCA) produces national mosaic of rainfall intensity on a grid of $1,400 \times 1,400\,\text{km}^2$ with a spatial resolution of 2.5 km^2 and a time sampling of 30 min. This product (Fig. II.7.1) covers mainly North and Center of Italy. It is worth emphasizing that the national surface rainfall intensity (SRI), used for this project, was not validated nor adjusted with rain gauges. The Italian SRI mosaic is composed of several RADARs managed directly by Regional Government, the Italian Air Force and some foreign countries such as France, Swiss,

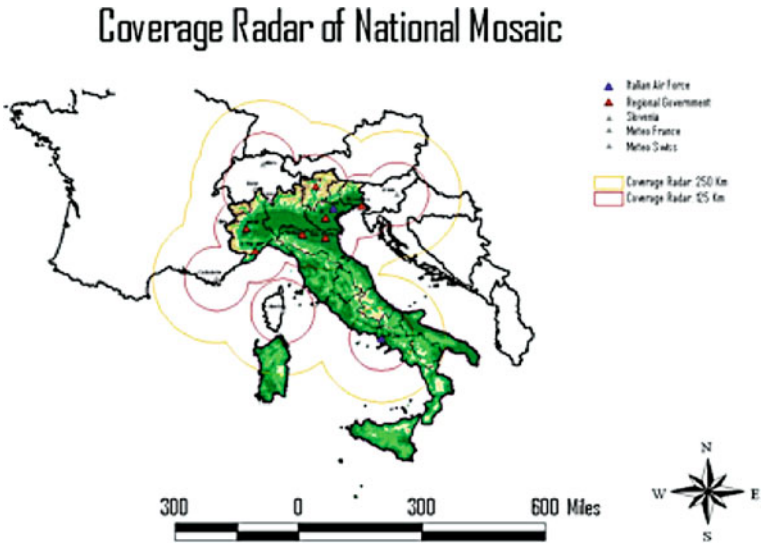

Fig. II.7.1 RADAR coverage

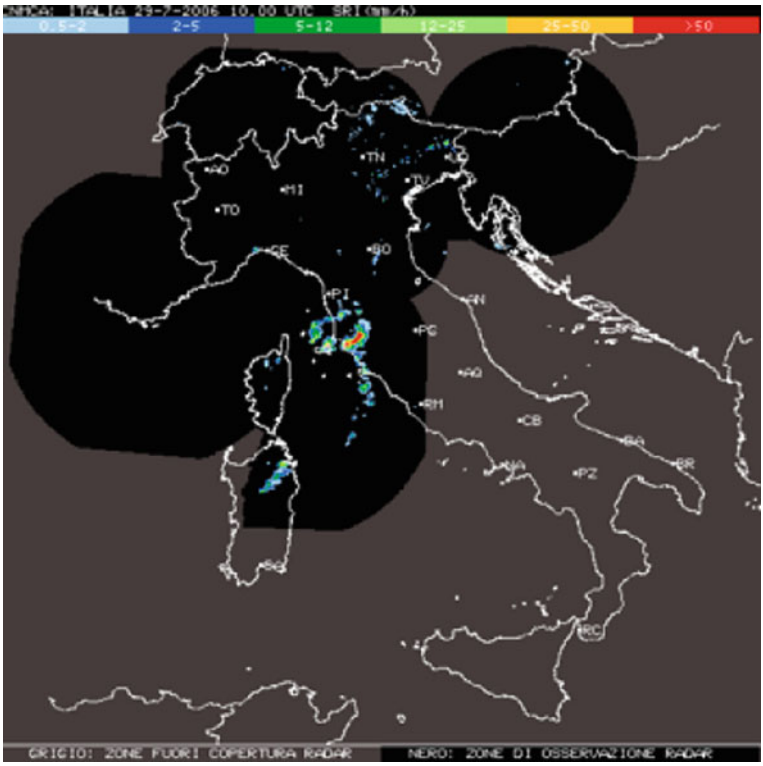

Fig. II.7.2 RADAR national mosaic (For color figure see online version)

and Slovenia (Fig. II.7.2). However for this study only Italian RADAR network was used. The most important technical features of the used RADAR systems are:

- C-band
  - Frequency: 3.900–5.750 GHz
  - Wavelength: 7.69–5.20 cm
- Doppler capacity up to 125 km;
- operation with polarimetric quantities (e.g., dual polarization);
- antenna with characteristics compatible with polarimetric observations;
- beam width = 1^{o};
- RADAR system remotely controlled with 24-h operability.

2.2 Rain Gauges

Rain gauge data acquisition and processing are performed at different temporal intervals ranging from 5 to 30 min. The observation collected by the National

Fig. II.7.3 Rain gauge distribution

Centers and Cumulate Maps of precipitation is made available within 45 min from the acquisition. Figure II.7.3 shows the distribution of the rain gauges over Italy and provides example of the available products.

2.3 Qualitative Comparison: RADAR–Rain Gauges

Since rain gauges and radars represent the main validation instruments for satellite-derived precipitation estimates, it was considered worth to evaluating how they compare to each other. This section describes the comparison of radar data aggregated on a SEVIRI grid (app. A) with individual rain gauges. Figures II.7.4 and II.7.5 show some of the inherent difficulties in using these kind of observations, especially for quantitative estimations. Some of the issues, described also in Sect. 3.4.1, are evident when comparing these two ground-based instruments. In particular:

- too many rain gauge observations are suspiciously reported to be 0 even where radar (as AMSU) sees precipitation;
- the rain gauge observations have not been convolved to the SEVIRI grid using the same convolving scheme used for radar data;
- often the radar temporal resolution (30 min) does not allow for a fair comparison with 10 min cumulated rain observed by the rain gauges;
- dependency of radar RR on observation radial distance from radar coordinates should be taken into account.

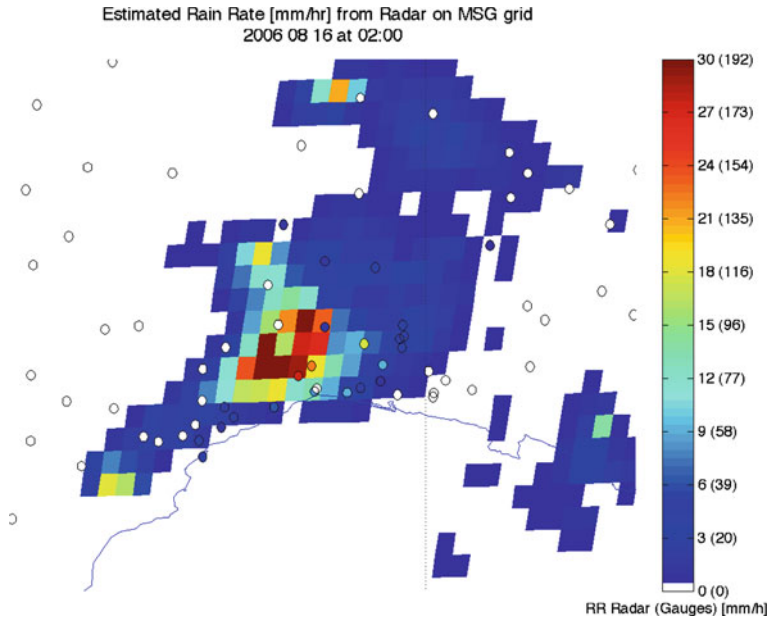

Fig. II.7.4 Radar-estimated RR on AMSU native grid between 02:00 and 02:30 UTC over the Gulf of Genova. RR-derived precipitation is described by the values next to the *colorbar*. The *colored circles* represent rain gauge observations. RR intensity estimated from 10 min cumulate precipitation measured by the gauges at 02:20 UTC is described by the values in parenthesis next to the colorbar (For color figure see online version)

3 Precipitation Retrieval from Microwave (AMSU) Data

3.1 AMSU Data

The advanced microwave scanning unit (AMSU) is a cross-track scanning microwave radiometer consisting of two separate modules: AMSU-A and AMSU-B. The first one has sounding channels in the water vapor (23.8 GHz) and oxygen absorption band complex (50 GHz) plus some window channels (at 31.4 and 89 GHz) and is dedicated mainly to the retrieval of temperature and water vapor profiles. AMSU-B has two window channels (at 89 and 157 GHz) and three channels in the water vapor absorption band at 183 GHz and is dedicated to the retrieval of ice cloud and precipitation (Grody et al., 2004). Being a sounding instrument, AMSU-A has a lower spatial resolution than AMSU-B. Channels and spatial resolutions are detailed in Table II.7.1. AMSU data used for this study were obtained from five platforms (NOAA 15, 16, 17, 18, and METOP-A) over the H-SAF domain (Europe), for a total of 10 overpasses per day, starting from February 1, 2006 (AMSU data from METOP-A were added after the platform launch). Examples of AMSU-B data at 89 and 157 GHz are shown in Figs. II.7.6 and II.7.7.

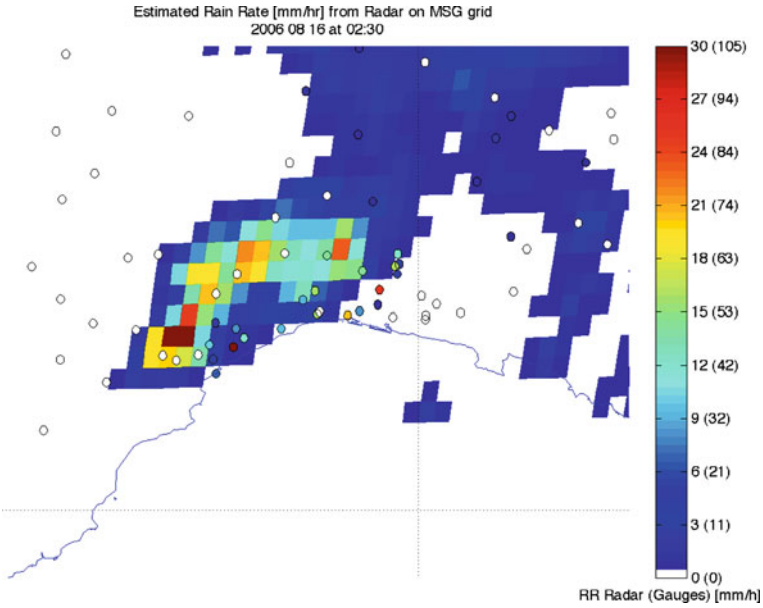

Fig. II.7.5 Radar-estimated RR on AMSU native grid between 02:30 and 03:00 UTC over the Gulf of Genova. RR-derived precipitation is described by the values next to the *colorbar*. The *colored circles* represent rain gauges observations. RR intensity estimated from 10 min cumulate precipitation measured by the gauges at 02:50 UTC is described by the values in parenthesis next to the colorbar (For color figure see online version)

Table II.7.1 AMSU-A and AMSU-B/MHS instrument characteristics

Satellite characteristics	AMSU-A	AMSU-B
Spatial resolution	3.3°	1.1
Nadir effective FOV	$50 \times 50\ \text{km}^2$	$20 \times 16\ \text{km}^2$
Scan edge effective FOV	$150 \times 80\ \text{km}^2$	$64 \times 52\ \text{km}^2$
Channels	23.8, 31.4, 50 GHz O_2 complex, 89.0 GHz	89.0, 150.0, 183 (WV absorption and) GHz

3.2 Precipitation Algorithm Theoretical Basis

The algorithm, hereafter referred to as precipitating clouds (PC) algorithm, uses two channels from AMSU-B. The main principle is that rainfall can be derived from the brightness temperature (BT) difference depression with respect to the background BT difference obtained in the absence of precipitation. In other words, the radiative cooling due to the scattering of the radiation by the ice particles overshooting precipitating convective clouds is taken as a rain indicator, and AMSU-B window channels (89 and 157 GHz) are used for deriving a so-called *Scattering Index* (*SI*):

$$s_{I1} = (T_{89} - T_{150}) - \Delta T_{bk\,(89-150)}$$

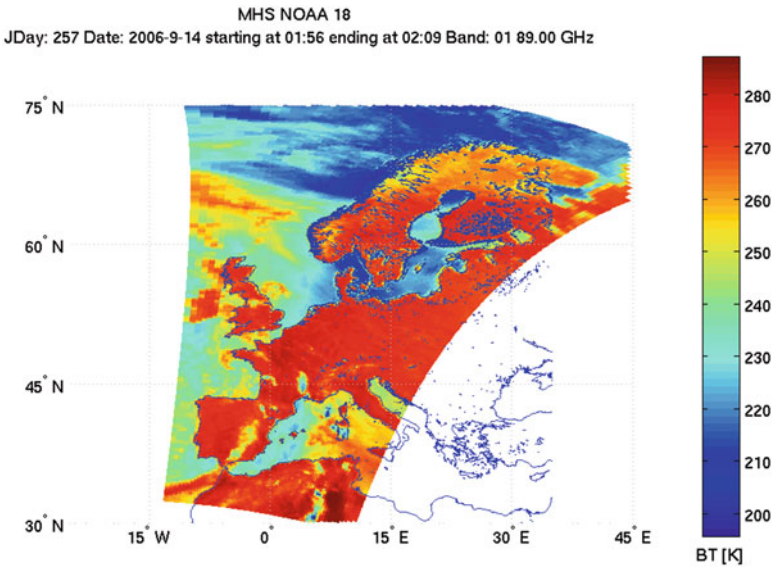

Fig. II.7.6 Example of AMSU-B at data 89 GHz

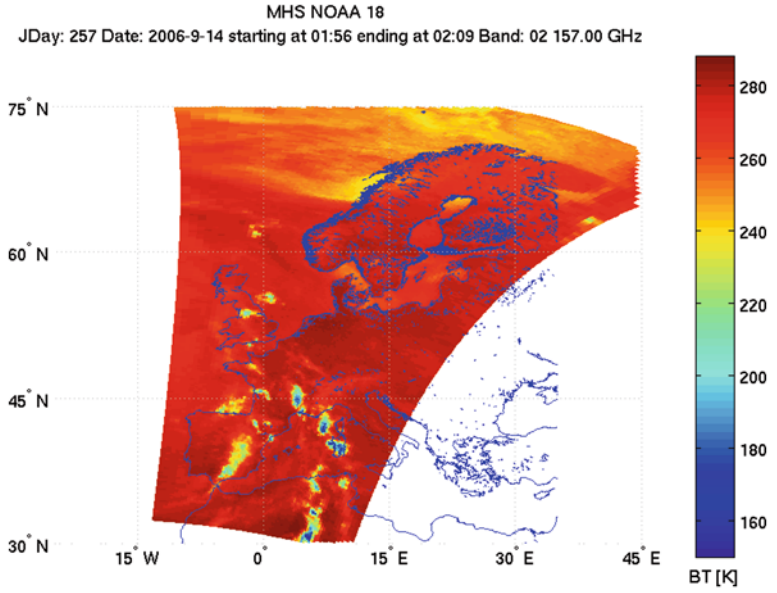

Fig. II.7.7 Example of AMSU-B at data 157 GHz

where T_{89}, T_{150}, for a specific field of view, are BTs at 89 and 150 GHz and $\Delta T_{bk\,(89-150)}$ is the corresponding difference of the BTs at 89 and 150 GHz in absence of precipitation. Detailed description of the algorithm can be found in Bennartz et al. (2002). Final product, obtained at AMSU-B resolution (Bennartz, 2000) is the likelihoods of rainfall classes (i.e., the probability that the rainfall falls within predefined ranges of RRs). Table II.7.2 shows the different classes used. Therefore, a given pixel will not be assigned a certain value but rather a set of probabilities for each of the four RR classes. The algorithm's approach is empirical. The relationships between the precipitation classes and the AMSU-derived scattering indexes and derived from the use of co-located, radar data, convolved at AMSU resolution. This approach allows to overcome the large systematic deviations that the current lack of knowledge about the microwave response to cloud/precipitation microphysics would introduce in case a detailed inverse modeling approach was chosen. This is especially true where surface characteristics are highly heterogeneous. The *precip-radiation database*, created by convolving rain gauge adjusted radar estimates, was used to calibrate the algorithm. The database is composed of thousands of couples of AMSU observations and related radar-derived precipitation classes. These data were collected during 8 months (April–November 1999) at Swedish Hydrological and Meteorological Institute (SHMI) and cover the Baltic Sea region. Due to the limited representativeness of this data set, the algorithm sensitivity, in the current implementation, does not allow for the discrimination of more classes.

It is worth emphasizing that the algorithm was tuned to perform optimally over northern Europe and it may not be exported to other regions straightforwardly. In fact, an adjustment to other climate regions is deemed necessary to re-define algorithm characteristic thresholds. It is also important to recognize that the database used to tune the algorithm must be statistically significant, and all the meteorological and climatological situations of interest must be conveniently represented. In fact, the problem of the representativeness of the database is a well-known problem in rainfall retrievals and may hamper the validity of the retrieval if not properly handled (Panegrossi et al., 1998; Bauer, 2001; Di Michele et al., 2003; Kummerow and Giglio, 1994). Finally, when using the *precip-radiation database*, one must be conscious that several errors are intrinsically taken on-board like the spatial and temporal collocation errors between radar data and satellite observations (due, for example, to temporal misalignments, to satellite navigation errors, to the different geometries of the observations).

Table II.7.2 Classes of different precipitation intensities used in this investigation (Bennartz, 2002)

Class	Type of precipitation	Minimum RR (mm/h)	Maximum RR (mm/h)
1	No precipitation	0.0	0.1
2	Risk of light precipitation	0.1	0.5
3	Light/moderate precipitation	0.5	5.0
4	Intensive precipitation	5.0	

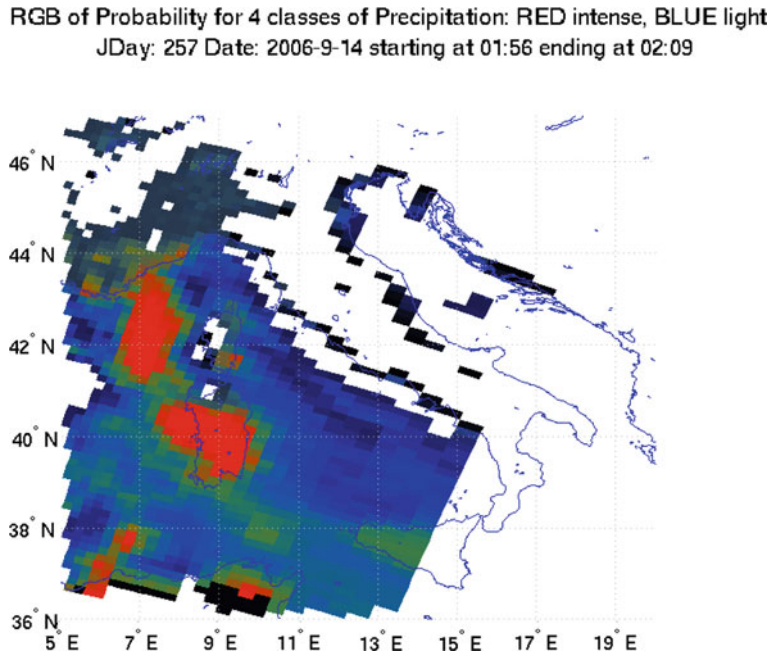

Fig. II.7.8 Example of PC standard RGB composite. The RGB is obtained mapping the probability of each pixel belonging to class 1 to *blue*, class 2 to *green*, and class 3 to *red*. The RGB obtained in this way shows high precipitation in *red* and low precipitation in *blue*. No precipitation is shown in *white*. The RGB conveys the full information about the likelihood of each pixel belonging to any of the four classes, however, it does not provide a single value per pixel and therefore can be used only for qualitative comparisons with radar or rain gauges (For color figure see online version)

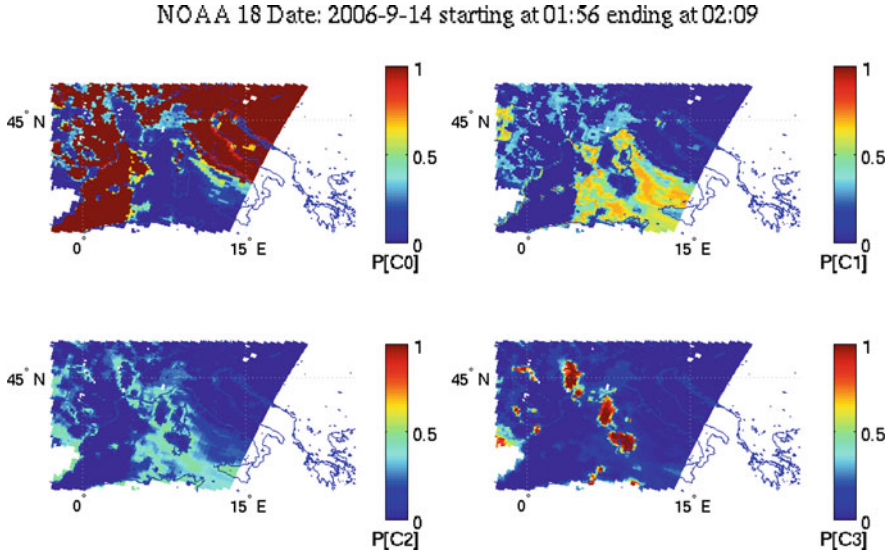

Fig. II.7.9 Example of likelihood for each individual class of precipitation as described in Table II.7.2

3.3 PC Products

From the PC output two products generated on the AMSU native grid are:

- likelihoods for four different intensity classes of precipitation;
- PC standard RGB composite (Fig. II.7.8). The RGB is obtained mapping the probability of each pixel belonging to class 1 to BLUE, class 2 to GREEN, and class 3 to RED. The RGB obtained in this way shows high precipitation in RED and low precipitation in BLUE. Absence of precipitation is shown in white. The RGB conveys the full information about the likelihood of each pixel belonging to any of the four classes, however, it does not provide a single value per pixel and therefore can be used only for qualitative comparisons with radar or rain gauges. Individual classed of probability are shown in (Fig. II.7.9).

In order to obtain point values of precipitation, the first PC product was further manipulated in two different ways:

- *Maximum probability approach* (Fig. II.7.10). The class with the highest probability is chosen. It is a straightforward approach, however it can be misleading: for

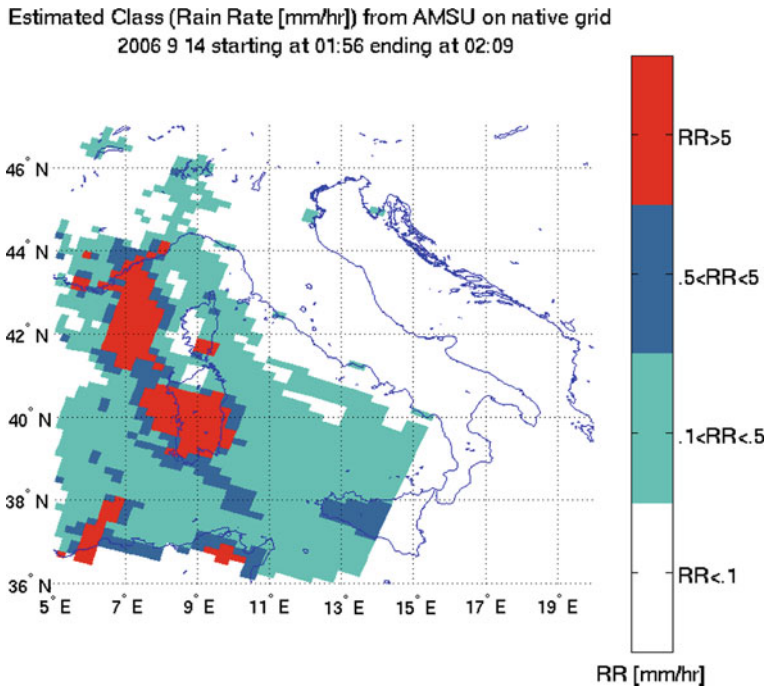

Fig. II.7.10 Example of original PC product: classification using the maximum probability approach. Classifying each pixel according to the maximum probability among the different classes provides a unique value (class), however, this value can be misleading when, for example, the probability, for a given pixel, is spread across two or more different classes. In this case the algorithm would still assign the pixel to one class and of the information regarding the probability distribution is lost

example if, for a given pixel, the probability across two or more different classes was uniform, the algorithm would still assigning one class only, and the information regarding the actual probability distribution among the different classes would be lost;

- *Weighted average RR approach* (Fig. II.7.11). The weighted average approach provides *an arbitrary* estimate of the RR according to the following equation: $\overline{RR} = \sum_{i=1}^{4} p_i \overline{rr}_i$ where p_i is the likelihood, and $\overline{rr}_i$ the mean RR value for class i. This quantity conveys the full information about the likelihood of each pixel belonging to any of the four classes, but the actual $\overline{RR}$ values are arbitrary as the mean value for each class (especially class four, intense precipitation) is set to a given value in an arbitrary way. In spite of this limitation, under specific circumstances, the representation is still useful for qualitative and quantitative comparisons.

Further developments of the PC algorithm, occurred after the realization of this study, introduced a new PC product for the instantaneous RR. However, the new product not used for the presented work is not discussed in this chapter.

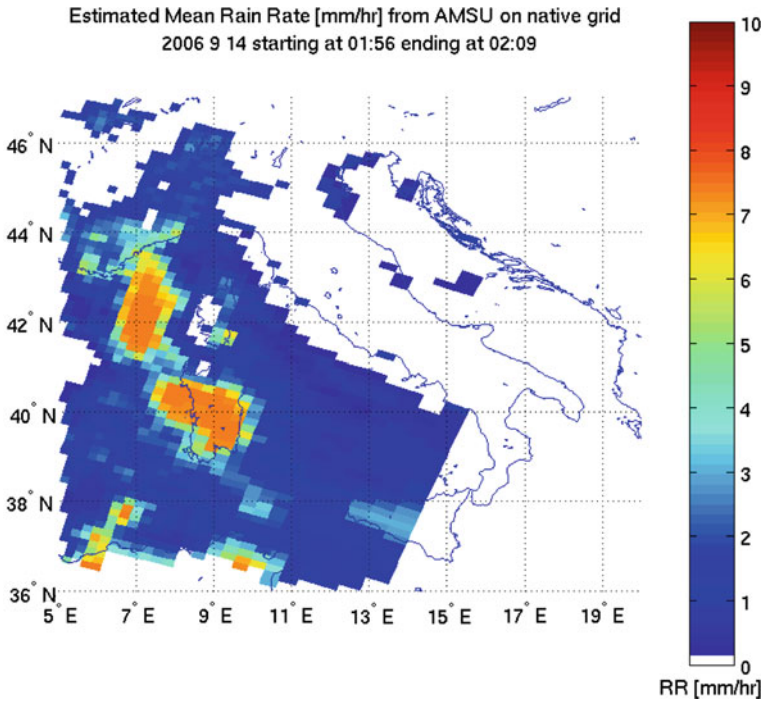

Fig. II.7.11 Example of original PC product: classification using the weighted average RR. The weighted average conveys the full information about the likelihood of each pixel belonging to any of the four classes, but the values above 5 mm/h are arbitrary as the mean value for class 4 (intense precipitation) was set to 10 mm/h in an arbitrary way. In spite of this, the representation is still useful for qualitative and quantitative comparisons

3.4 PC Validation

3.4.1 Qualitative Validation: PC-GAUGES

Figure II.7.12 and II.7.13 shows that a simple comparison, between PC-weighted average RR and the rain gauge observations, does not provide conclusive evidence useful for the estimation of the PC accuracy. This might be explained by the following considerations:

- too many rain gauge observations are *suspiciously* reported to be 0 even where AMSU (as radar) sees precipitation;
- rain gauge observations were not convolved at AMSU resolution; and
- the impact AMSU geolocation uncertainty should be carefully estimated.

In spite of these difficulties the 10 min (cumulated rain) temporal resolution of the rain gauge observations and their dense spatial distribution make them potentially useful for qualitative and quantitative estimate of the PC accuracy.

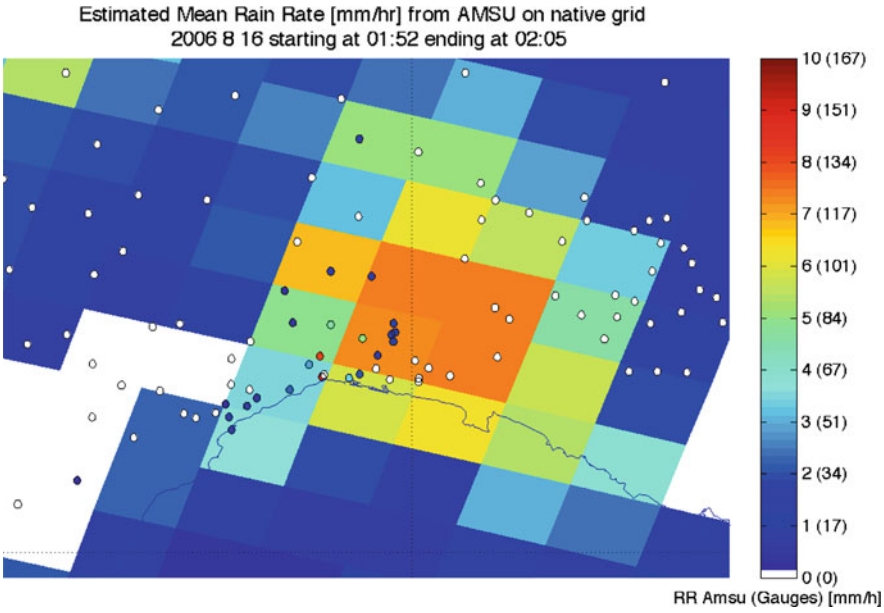

Fig. II.7.12 PC-weighted average on AMSU native grid at 01:52 UTC over the Gulf of Genova. AMSU-derived precipitation is described by the values next to the *colorbar*. The *colored circles* represent rain gauges observations. RR intensity estimated from 10-min cumulate precipitation measured by the gauges at 02:00 UTC, is described by the values in parenthesis next to the *colorbar* (For color figure see online version)

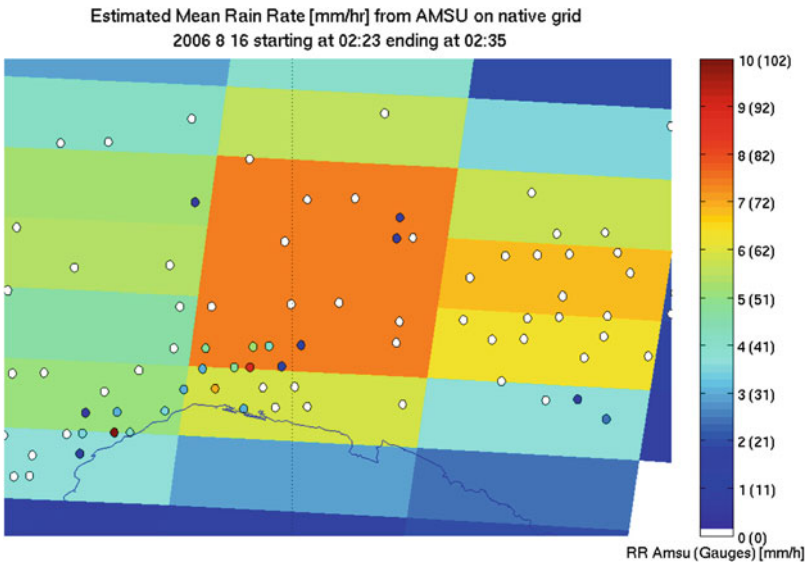

Fig. II.7.13 PC-weighted average on AMSU native grid at 02:35 UTC over the Gulf of Genova. AMSU-derived precipitation is described by the values next to the *colorbar*. The *colored circles* represent rain gauges observations. RR intensity estimated from 10 min cumulate precipitation measured by the gauges at 02:30 UTC is described by the values in parenthesis next to the *colorbar* (For color figure see online version)

3.4.2 Quantitative Validation of PC with Radar Data on AMSU Grid

The quantitative validation of the original PC algorithm, applied to Southern Europe, was done for about 43,000 observations taken in 7 different days by the NOAA 16 and 18 satellites. It was performed using radar data convolved on the AMSU grid as shown in Fig. II.7.14. The results were compared in two ways:

1. AMSU precipitation classes (max probability approach) were compared to radar-derived classes of precipitation, pixel by pixel on AMSU native grid.
2. AMSU re-calculated classes (weighted average approach) were compared to radar-derived classes of precipitation, pixel by pixel on AMSU native grid, according to the following procedure:

   (a) AMSU-derived RR was calculated using the weighted average of the likelihoods. A mean RR value was assigned to each class (as described by third point of Sect. 3.3) and
   (b) weighted averages of RR were classified again according to Table II.7.2.

This methodology was required because the weighted average is an arbitrary estimate (in particular, the mean value of the intense precipitation class is arbitrary), and the one based on the maximum likelihood does not take into account

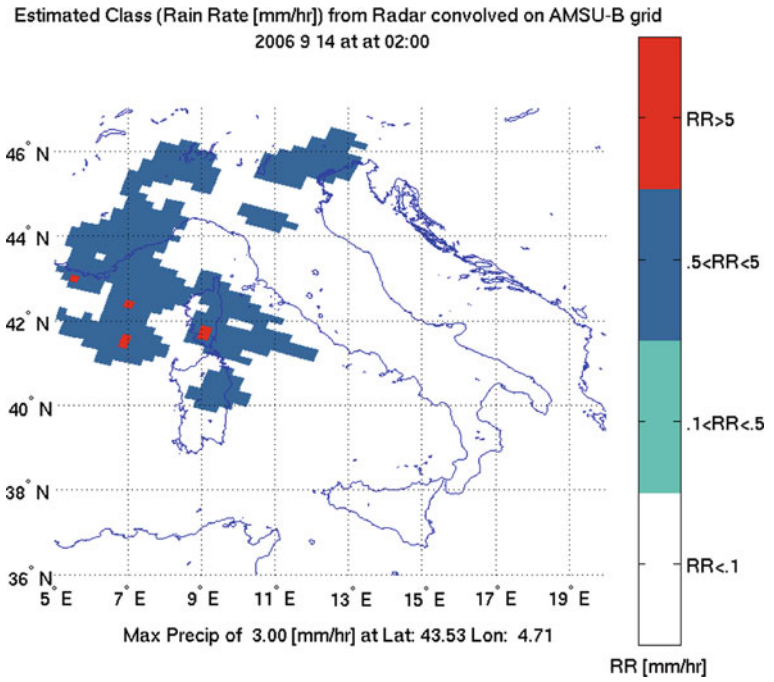

Fig. II.7.14 Example of radar data convolved at AMSU-B spatial resolution and binned using the same classification thresholds used by the PC algorithm

the probability distribution among the different classes but only the maximum probability.

Radar data were convolved on AMSU grid and classified according to Table II.7.2 and the contingency tables were then calculated for all the selected overpasses. These procedures do not take in account several of the issues discussed in the previous sections but still provide some useful information on the performances of the PC algorithm over the Mediterranean area. The results presented in Tables II.7.3, II.7.4, and II.7.5 indicate that:

- In both cases (max probability and weighed average) PC misclassified several pixel assigning them to class 2 and 3 ($0.1 < RR < 5$ [mm/h]) while according to the radar the pixels were belonging to class 1 (no precipitation) as showed in Table II.7.5. This misclassification issue appeared to be more evident for daytime passes (Table II.7.3) than for nighttime ones (Table II.7.4);
- Several pixels were classified as class 4 ($RR > 5$ [mm/h]) by PC while according to the radar they were belonging to class 3 ($0.5 < RR < 5$ [mm/h]). The issue is due to the fact that radar, with increasing distance, tends in general to underestimate RR intensity. The problem is also due to the arbitrary mean value associated to class 4 in the intermediate step for the PC product when the weighted average RR was calculated.

Table II.7.3 Contingency table for daytime only for the max probability approach and for the weighted average approach (in parenthesis). PC classification are on the rows while radar estimations are on the columns

PC/RADAR	*R*1	*R*2	*R*3	*R*4
C1	93.69 (95.02)	4.74 (3.86)	1.52 (1.10)	0.05 (0.01)
C2	66.05 (93.66)	21.21 (4.03)	12.15 (2.11)	0.73 (0.20)
C3	23.66 (63.33)	36.62 (19.79)	37.22 (16.03)	1.85 (0.84)
C4	3.40 (0)	16.54 (5.81)	68.98 (71.32)	5.82 (22.86)

Table II.7.4 Contingency table for nighttime only for the max probability approach and for the weighted average approach (in parenthesis). PC classification are on the rows while radar estimations are on the columns.

PC/RADAR	*R*1	*R*2	*R*3	*R*4
C1	92.47 (93.52)	5.34 (4.70)	2.17 (1.76)	0.01 (0.01)
C2	53.50 (82.75)	28.78 (13.55)	16.99 (3.70)	0.73 (0.00)
C3	21.69 (50.87)	37.03 (26.24)	39.41 (21.70)	1.85 (1.18)
C4	13.60 (12.10)	17.67 (12.81)	62.91 (69.39)	5.82 (5.69)

Table II.7.5 Contingency table for day- and nighttime for the max probability approach and for the weighted average approach (in parenthesis). PC classifications are on the rows while radar estimations are on the columns. Overall the radars detected 37,044 FOVs with no precipitation (*C*1), 3,427 of *C*2, 2,464 of *C*3, and 171 of *C*4; PC detected 36,740 FOVs with no precipitation (*C*1), 3,955 of *C*2, 1,219 of *C*3, and 1,192 of *C*4

PC/RADAR	*R*1	*R*2	*R*3	*R*4
C1	93.11 (94.28)	5.01 (4.28)	1.82 (1.42)	0.03 (0.01)
C2	62.14 (88.89)	23.56 (8.20)	13.65 (2.8)	0.63 (0.10)
C3	23.05 (59.79)	36.75 (21.62)	37.90 (17.63)	2.29 (0.94)
C4	7.80 (6.03)	17.03 (9.46)	66.35 (70.31)	8.81 (13.91)

Both issues are well understood and they were expected in the application of the PC algorithm to Italian areas. For the described validation exercise the results obtained were, on average, 18% worse, with a peak of 58% for class 4, with respect to those obtained by Bennartz (2005). The discrepancies can be furher explained considering that:

- the radar data used in the validation were not gauge adjusted, underestimation of precipitation from radar data was, therefore, expected;
- the algorithm was trained only with North European radars and for high latitude climate regimes;
- in his validation Bennartz discriminated between land and water pixels and excluded coastal regions, which were less relevant over northern Europe, than for the Italian case;

- over coastal (and in general heterogeneous) and non-vegetated pixels the current scheme for background temperature estimation does not provide optimal results, this issue appears to be more evident over Italy;
- class 4 pixels over northern Europe are much less frequent than over southern Europe, therefore the data set used to calibrate the algorithm might not be, at this stage, enough representative for the Italian cases.

It is worth mentioning that overall the radars detected 37044 FOVs with no precipitation ($C1$), 3427 of $C2$, 2464 of $C3$, and 171 of $C4$; PC detected 36740 FOVs with no precipitation ($C1$), 3955 of $C2$, 1219 of $C3$, and 1192 of $C4$.

3.5 Improvements to the PC Algorithm

As described in Sect. 3.2, and as shown in Sect. 3.4.2, the performances of the PC algorithm largely rely on the computation of a realistic radiative background. In fact, the rainfall estimation is based on the deviation of the measured BT differences, at 89 and 150 GHz, with respect to the background BT differences (i.e., the ones that would be measured in non-precipitating conditions). In its original implementation, the background BT was computed dynamically over a wide region surrounding the pixel of interest (2 degrees by 2 degrees). This technique is simple and efficient but has several drawbacks, since the possibility that the resulting BT is contaminated by precipitation and/or by heterogeneous backgrounds is extremely high. As a consequence, an effort was devoted to developing a new technique for deriving background BTs: a grid of clear sky pixels was built by making use of a certain number of AMSU overpasses. For a given time interval preceding the one of interest, AMSU data were projected onto a fixed regular grid (the SEVIRI one was used). This projection was done by using the remapping process described in Appendix A. The warmest AMSU clear sky BTs at 89 and 157 GHz, among all the overpasses within a certain time window (4 days in this study), were retained and mapped onto the the higher resolution SEVIRI fixed grid.

This approach provides good results but is not optimal. In fact, over the (radiatively) hot land surfaces, scattering cooling from precipitation causes BTs to decrease. Thus, hot backgrounds easily mark clear sky pixels. However, the same reasoning cannot be applied over ocean surfaces. In fact, since sea surface emissivity at 89 and 157 GHz varies between 0.6 and 0.7, ocean backgrounds are always radiatively cold. Convective events still cause radiative cooling by scattering, however, water vapor and light precipitation can warm the measured BTs with respect to the clear sky signatures. Therefore, hottest pixels might not necessarily correspond to clear sky ones. However, since the warming varies with the wavelength (the 89 GHz being more sensitive to water vapor), the differential signal should in theory be kept as an indicator of clear sky pixels. The SI should be maximum at clear sky (due to the differences in SSE) and minimum during convective precipitation (due to the enhanced scattering at 157 GHz than at 89 GHz). The differential

discrimination was attempted but caused significant errors by detecting light precipitation over clear sky ocean regions, therefore, was not adopted for this study as deeper investigation is needed for its use.

The time window of 4 days used for the computation was proved to be large enough to allow for clear sky conditions to be found for every scene pixel and short enough to remain within background conditions that are representative of the overpass under examination.

In this regard, it is worth noting that a considerable impact was observed from night/day variations (implying deviations as large as 30 K on the background BTs), a fact which suggested to restrict the computation of the background temperatures to overpasses within a few (6 in this study) hours from the time of interest. In order to avoid problems linked to the instrument calibration, separate background calculations were also done for the different satellites.

The described approach resulted in a considerable improvement on the computed clear sky BTs, and this had a significant impact on the derived precipitation estimates as shown in Figs. II.7.15 and II.7.16. The improvements are visible especially over coastal regions (North Africa) and over non-vegetated land (Sicily and Sardinia) where with original scheme, false precipitation was detected in clear sky

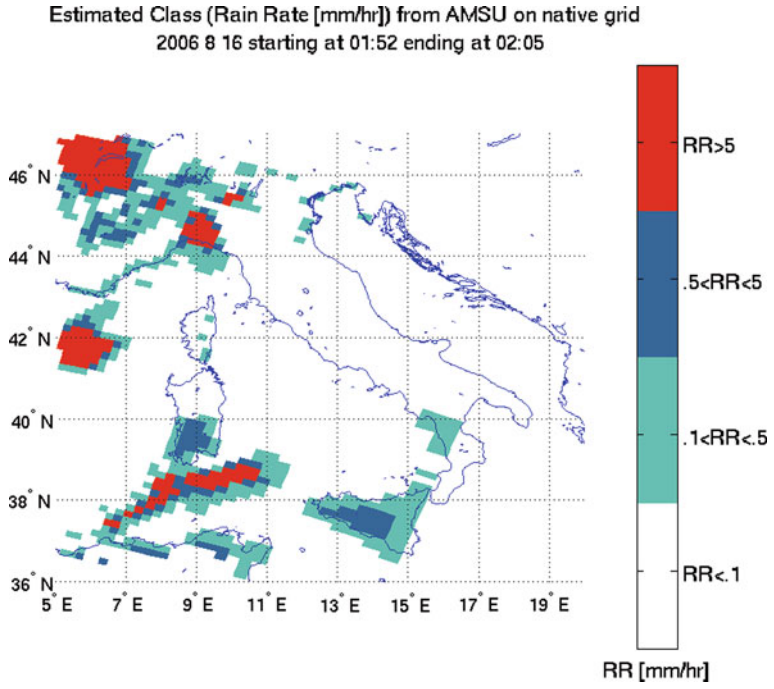

Fig. II.7.15 NOAA 18 16-08-2006 at 01:52 UTC: PC retrieval obtained with original estimation of background BTs. Light precipitation is erroneously detected in clear sky regions (over Sicily, Sardinia, and North Africa), Fig. II.7.21

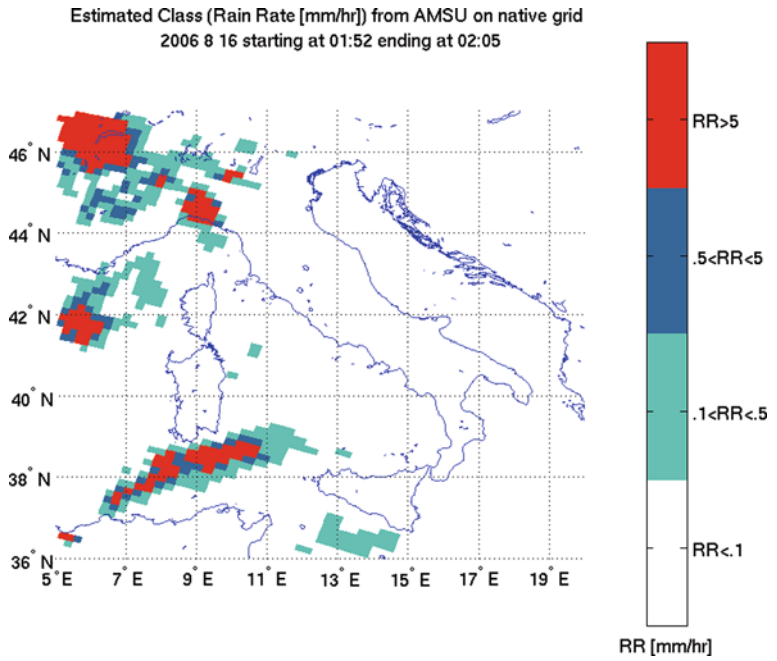

Fig. II.7.16 NOAA-18 August 16, 2006 at 01:52 UTC: PC retrieval obtained with the estimation of background BTs derived from previous time-coincident, same-platform overpasses. No precipitation is detected in the clear sky regions over Sicily, Sardinia, and North Africa

regions (Fig. II.7.21), whereas with the new scheme, the misclassification tends to disappear. SEVIRI data in Fig. II.7.22 show the improvements of the new approach even over ocean (Fig. II.7.17) with respect to the original version of the PC algorithm for a different NOAA 18 overpass (September 14, 2006 at 01:56 UTC) as shown in Fig. II.7.10. For the sake of clarity, Figs. II.7.6, II.7.8, II.7.9, and II.7.10, show examples obtained with the original version of the PC algorithm.

The new implementation also allowed for an improvement in the estimation of precipitation over very heterogeneous surfaces (namely over coastal areas): the fact that the background BT selection was done by considering several overpasses and on a fixed, high-resolution grid (the SEVIRI one is used), the heterogeneity of the background BTs was better retained, thus allowing a mitigation of the estimation errors.

A further possible improvement for this algorithm could consist of a smoothing of the computed background BTs before ingesting them in the retrieval scheme. In fact, being computed over different overpasses (and therefore even from different observation angles) the radiative backgrounds may present some important discontinuities among adjacent pixels (e.g., differences as large as 10% could derive from the different scan angles of the retained clear sky pixel) that could impact on the final rain estimation.

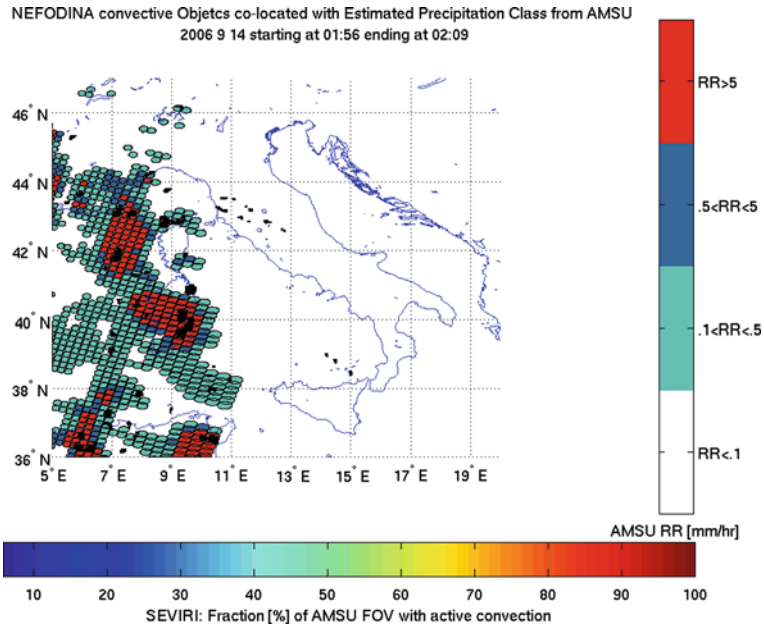

Fig. II.7.17 NOAA-18 September 14, 2006 at 01:56 UTC: PC retrieval obtained with improved estimation of background BTs derived from previous time-coincident, same-platform overpasses. No precipitation is detected in the clear sky regions over Sicily and over ocean. In this figure PC values are mapped onto actual AMSU effective FOVs (EFOVs) calculated according to Bennartz (2000)

3.6 Errors and Uncertainties

The validation procedure described in Sect. 3.4.2 highlighted some issues specific to the PC product. These issues, discussed in the following subsections, were accounted for the implementation of the merging algorithm described in Sect. 5.1.

3.6.1 AMSU Geolocation Uncertainties

AMSU data suffer from considerable geolocation errors, depending on the platform. NOAA scientists have evaluated these errors by analyzing the discontinuity in correspondence of coastline in clear sky conditions. Errors were found in both the along and the cross-track direction. The displacement was quantified as large as 4.2 and 5.5 km (cross-track and along-track respectively) for NOAA-17 and 3.2 km and −16.4 km for NOAA-18. As for NOAA-18, an example of the considerable displacement (two pixels) that was evidenced on the Red Sea with such a technique is clearly visible in Fig. II.7.18.

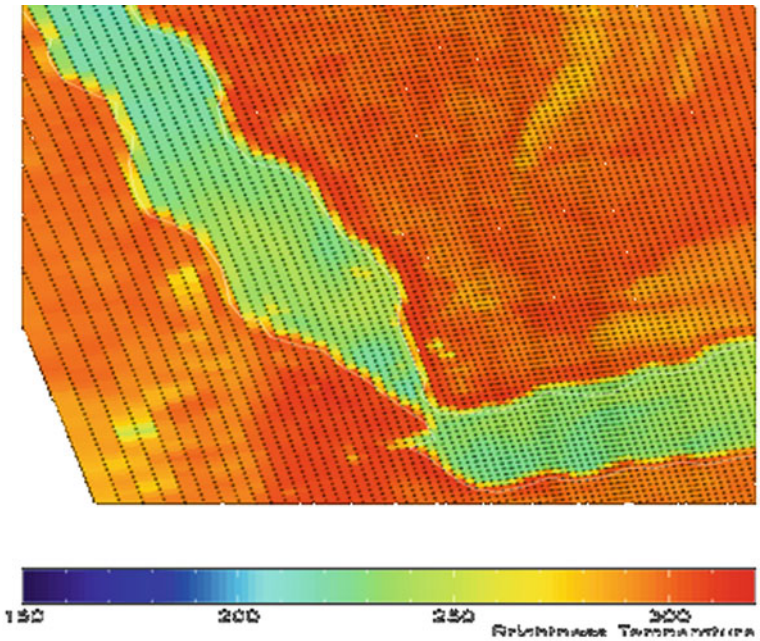

Fig. II.7.18 NOAA-18 AMSU-B image at 89 GHz over the Red Sea (figure exerted from http://www.orbit.nesdis.noaa.gov/smcd/spb/n18calval/calval/mhs.html#mhsgeo)

3.6.2 Scan-Dependent Uncertainties

The fact that AMSU is a cross-track scanning instrument has a major impact on the relative quality of the resulting rainfall estimations, due to several reasons. Different viewing geometries correspond to different sensed areas and different radiative properties. The effect of atmospheric optical thickness, surface emissivity, and hydrometeor particle emissivity, on observed BTs, all depend, to different extent, on the viewing geometry. Even purely geometrical effects related to the change in the equivalent area of the sensed portion of the cloud play an important role in this respect. In addition, off-nadir slanted observing geometries may introduce important geometrical distortions in the rain cell localization at surface level, as schematically sketched in Fig. II.7.19. At the frequencies of interest, the source of the (scattering) signal is not the surface rainfall layers, but the ice layers aloft. At nadir, the surface rainfall can be assumed co-located with the BT scattering signal.[1] However, when observing through slanted views, significant displacements may exist between the location of the scattering source location and the effective

[1] This is true only in the hypothesis that the convective towers extend vertically under the sensor field of view. However, horizontal shears may introduce possible shifts and generate tilted events (see for instance Hong et al., (2000) about a tilted convective event observed from the TRMM precipitation radar)

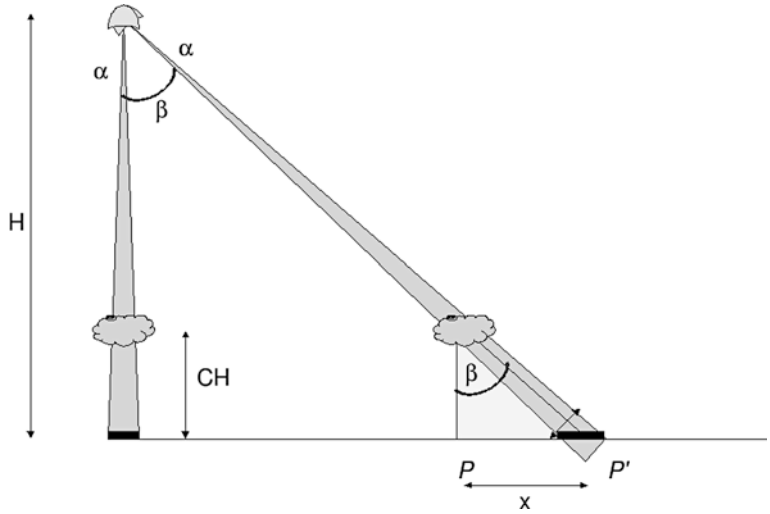

Fig. II.7.19 Schematic representation of the localization error for surface rainfall rate position. At slant angle β, rainfall is located in correspondence of position P, whereas the current location should be P'. The corresponding shift x is referred to as the *parallax error*

location of the convective rain at surface level. This displacement is often referred to as the *parallax error*, and it increases proportionally with the altitude of the cloud and with the observation angle. Theoretically, a graupel cloud situated at 10 km height could be located almost 10 km away from the real surface RR location, if sensed at maximum scan edge.

A straightforward correction could be therefore attempted once the corresponding cloud top height is supposed to be known. However, from using AMSU brightness temperatures, there is no mean to derive this piece of information.[2] Therefore an automatic correction for such a displacement is not deemed possible: estimating the height of the main source of the scattering signal (i.e., the center of gravity of the *generalized weighting function*) seems not reasonable due to the complexity and the uncertainties related to the characterization of the micro and macro-physical properties of the precipitating cloud.

Another scan-dependent source of error is due to the calibration of the instrument itself: NOAA scientists have observed an asymmetric behavior of the sensed radiances across the scan lines which amounts to more than 5 K

- http://www.orbit.nesdis.noaa.gov/smcd/spb/n18calval/calval/mhs.html#mhsgeo
- http://www.orbit.nesdis.noaa.gov/smcd/spb/mirs/validation/characterization.html

[2]Or in any case without introducing significant errors. As an example, the possibility to use SEVIRI-derived cloud top heights was discarded due to the fact that the cloud top height sensed by the IR channels might in general be much higher than the source of scattering signature characterizing the microwave frequencies and also to the time-shift that in any case would exist between the two observations.

The main impact, however, is due to the fact that the dimensions of the sensed area vary by more than 200% from nadir to scan edges. According to Bennartz (2000), the relationship between EFOV and scan angle, both in cross-track and along-track direction, can be modeled through the following interpolating formula:

$$\begin{aligned} \mathrm{EFOV(across-track)} &= 79.08 + 2.84\, m - 14.78\, m^{0.66} \\ \mathrm{EFOV(along-track)} &= 28.72 - 0.9\, m + 0.094\, m^{1.5}, \end{aligned}$$

where m is the scanning position. The cross-track EFOV passes from 15 km at nadir to more than 50 km at scan edge. Within such a variation, the heterogeneity of the sensed scene (and the possibility that the observed precipitation event "fills" the EFOV homogeneously–the so called beam filling problem, see for instance Kummerow (1998)) augments considerably. Everything that falls inside the sensed area is integrated and filtered in the sensor view, but the significance of the resulting information decreases with the heterogeneity of the observed scene. At scan edges, the probability to filter out and even loose narrow isolated sub-pixel convective cells increases considerably.

From all the considerations mentioned above, it should be clear that a different degree of uncertainty should be associated to AMSU measurements, proportionally depending on the scan angle: as a consequence, rainfall estimations at nadir are more reliable than the ones located along scan edges. Instead of attempting risky (and, at this stage, subjective) corrections to the estimates, we propose, as future work, that a scan-dependent confidence index should be associated to AMSU measurements, being maximum at nadir, and decreasing with the scanning angle. The confidence index should be taken into account when evaluating the performances of AMSU-derived rainfall rates.

4 Convection Detection from SEVIRI Data (Nefodina)

4.1 Data Description

SEVIRI is a scanning radiometer which operates on Meteosat Second Generation (MSG). It provides data in visible, near infrared, and infrared channels. Full spatial resolution in 12 spectral channels. *Nominal Coverage* includes Europe, Africa and locations with satellite elevation greater than or equal to 10°. The IR channels are designed with three narrow band detector elements per channel to scan the Earth every 3 km at the sub-satellite point. The high-resolution visible (HRV) channel provides measurements with resolution of 1 km.

The full Earth disc image is obtained after 1,250 scan line steps (south–north direction) of 9 km SSP per line step. The satellite spins at 100 rpm allowing to complete (east–west direction) a full image in about 12.5 min. The Earth observation repeat cycle is of 15 min. These real-time data are processed to Level 1.5, i.e., are

corrected for radiometric and geometric non-linearity, before onward distribution to the user. All SEVIRI data are available through EUMETCast.

4.2 Algorithm Description

Nefodina (Puca et al., 2005, 2009) is an automated tool, developed at the Italian Meteorological Service, which uses SEVIRI data to detect convective cloud systems to monitor their life cycle and to forecast their development. The derived product, using a varying threshold method in infrared window 10.8 μm and absorption channels 6.2 and 7.3 μm, allows for the identification of the convective object (CO) with a top BT lower than a temperature threshold of 236 K.

The detection method relies on the following basic assumptions:

- the temporal and spatial satellite data sampling is compatible with the corresponding scales of the phenomena;
- the evolution of the cloud top temperature joined with the water vapor amount in the medium and high troposphere represent a good tracer of convective cells;
- it is possible to represent the life cycle of the convective cell with a linear combination of cloud top temperature and the water vapor amount in the high troposphere.

The nefodina algorithm flow chart is reported in Fig. II.7.20.

4.3 Product Description

The nefodina product consists of a portable network graphic (PNG) image of the last available SEVIRI infrared (10.8 μm) image where the detected cells, their development, and their tracking are color coded to give a quick overview to the forecaster (Figs. II.7.21 and II.7.22). This output image is associated to an ASCII file where the minimum, medium, and modal BT of the 10.8, 6.2, and 7.3 μm channel is reported with shape, slope area, and other information relative to the detected COs.

4.4 Nefodina Validation

4.4.1 Qualitative Comparison of Nefodina CO with Radar Data

As previously done for radar and rain gauge data, the nefodina-detected COs superimposed to radar-derived RR are showed in Fig. II.7.23. The grey diamonds represent the centers of the SEVIRI FOVs labeled as convective by nefodina, while the black circle represent the positions of the COs after a rigid shift which maximize

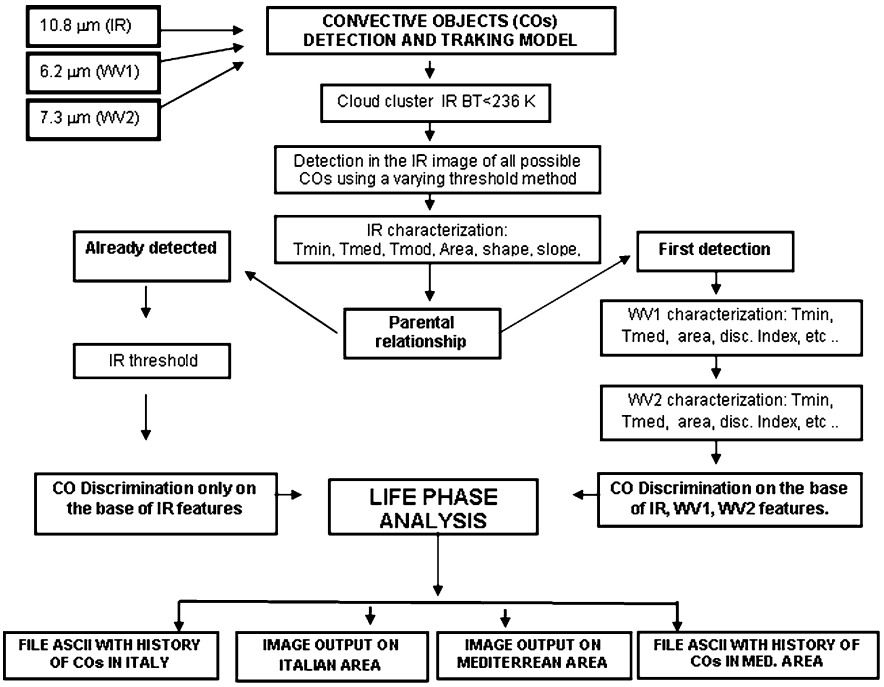

Fig. II.7.20 Nefodina flow diagram

the radar-detected precipitation within each CO. The misalignment of the original CO positions with respect to the radar map looks consistent for the different COs. Misalignments are mostly due parallax and geolocation errors. While Sect. 4.5.1 introduces a methodology to properly correct for parallax errors, the actual approach selected to mitigate the misalignment between AMSU, SEVIRI, and radar data was based on a rigid shift which maximizes the precipitation within each object and it is described in Sect. 5.1.

4.4.2 Quantitative Validation

Validation on the detection efficiency of nefodina was performed, following the idea that a CO during its life has an electric activity. Often this happens during the mature stage. The validation was based indeed on the observation of lightning measured by the lightening network (LN) of the International Association of Forensic and Security Meteorology (IAFMS) during the life of the CO and it was conducted on a set of 12,000 data uniformly selected along 1 year of MSG data. Probability of detection (POD) and false alarm rate (FAR) were obtained, respectively, equal 0.84 and 0.17. Sixty percent of the CO were detected and classified as convective by nefodina 30–45 min (2–3 MSG slot) before any electric activity was measure by LN.

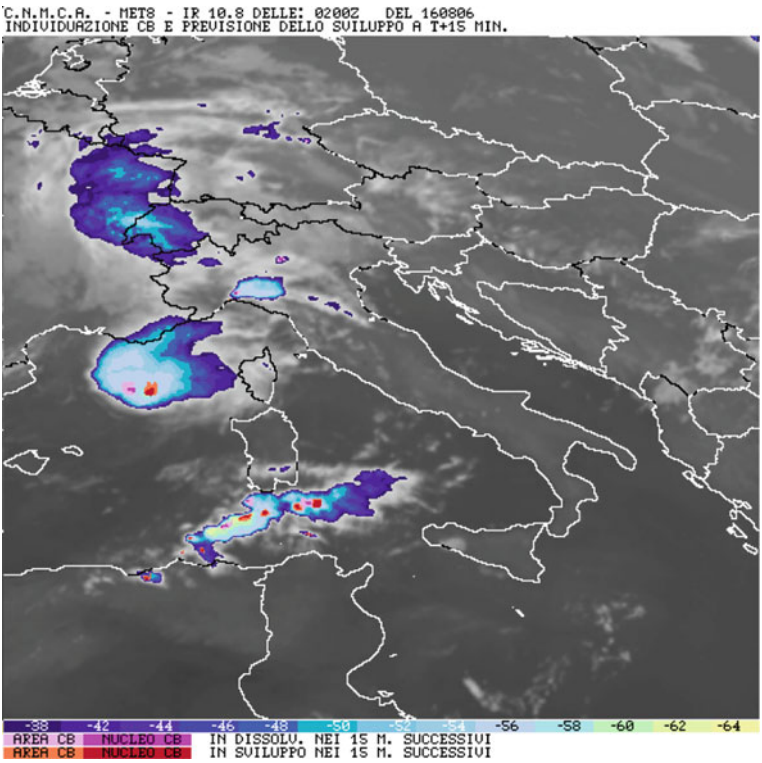

Fig. II.7.21 Example of nefodina product at 02:00 UTC on August 16, 2006. The colorbar shows the cloud top temperature. The red pixels show increasing CB, while the pink pixels show the decreasing CB (For color figure see online version)

4.5 Errors and Uncertainties

In this section the only source of uncertainty described refers to the parallax errors because a full validation of nefodina is beyond the scope of work presented in this chapter.

4.5.1 Parallax Error

The concept of parallax error (i.e., the mislocation, on the Earth surface, of rain cells due to slanted satellite observations) was already introduced in Sect. 3.6.2 for AMSU. However, even SEVIRI rain products may be affected by such a problem, as already noticed by Davenport et al. (2007). In fact, the SEVIRI camera is observing the Earth with a spherical geometry centered in the Gulf of Guinea (approximately at 0° latitude and longitude). The sensor viewing angle increases with the radial distance from the nadir point. The viewing angle increases as function of the geographical location, introducing potential distortions and pixel enlargement (the

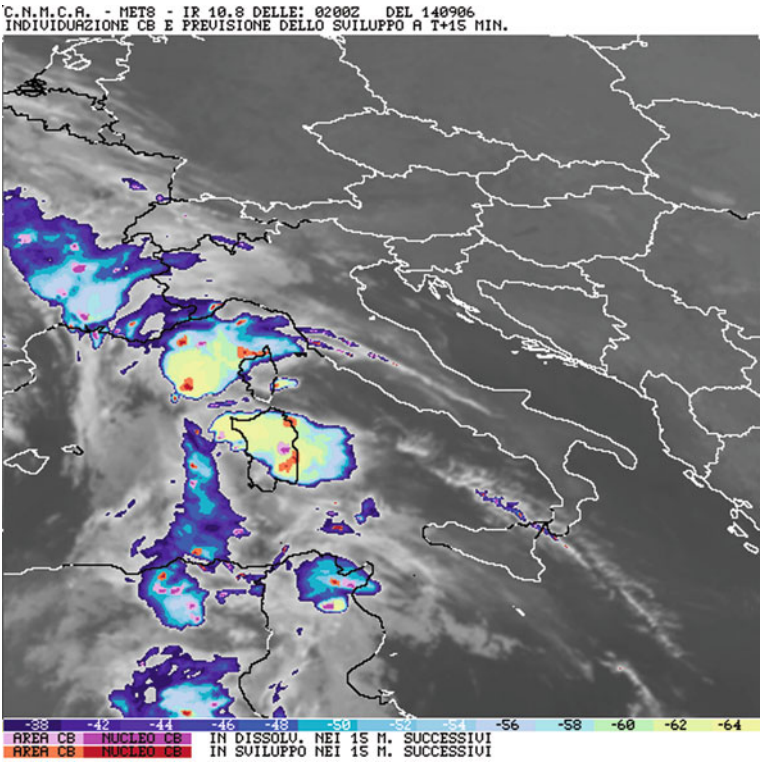

Fig. II.7.22 Nefodina September 14, 2006 at 02:00 UTC (For color figure see online version)

effective pixel size increases radially from the nadir point). Complete details about SEVIRI are provided by Wolf et al. (1999).

For the purposes of this study, the SEVIRI slanted observing geometry may have an impact in that the location of the observed signal source (cold pixels associated to convective events and possibly to the largest cloud top heights) may be shifted by several kilometers with respect to the effective location of the precipitation at the surface. Therefore, the convective pixels are relocated so that are in correspondence with the effective location of the surface rain. From Wolf (1999), we computed such a displacement as function of the latitude and longitude of the observation (radial distance from nadir sub-satellite pixel). As an example, for a 10 km height cloud top in the Mediterranean, we obtain a displacement as large as 7 km in the radial direction. It must be highlighted, though, that this calculation relies on the assumption that the observed event is perfectly vertical and that horizontal shears are minimal. Correcting SEVIRI precipitation products for the parallax did not account for the whole misplacement of the convective cell location with respect to the region of high radar precipitation. However, the correction did lead to improved geolocation with respect to radar data (Fig. II.7.24)

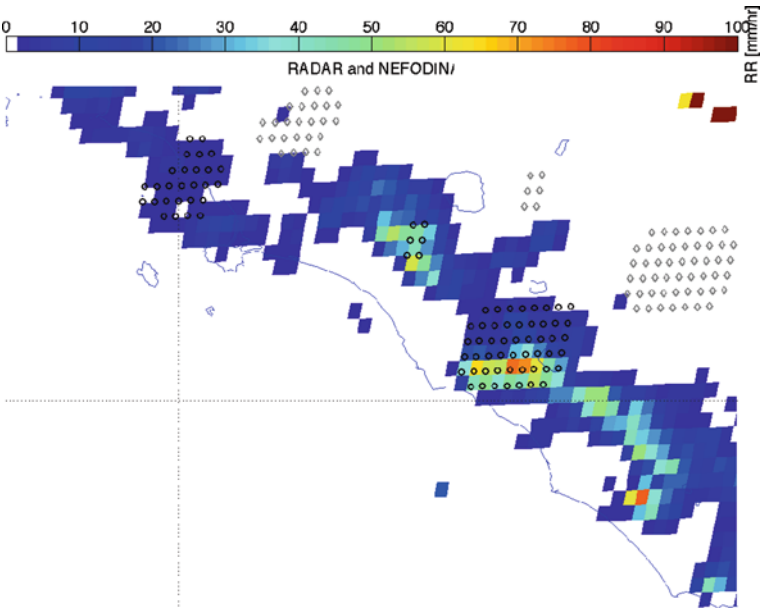

Fig. II.7.23 Comparison of nefodina-detected CO and radar RR for April 24, 2008 at 15.30 UTC. *Grey diamonds* represent the original COs detected by nefodina, the *color-map* represent the radar rain rate and the *black circles* indicate the optimal position of the COs after re-colocating them according to the procedure described in Sect. 5.3. (For color figure see online version)

5 Convective Precipitation Retrieval from Combined AMSU and SEVIRI Data

5.1 Algorithm Description

In the proposed approach AMSU PC data were co-located with nefodina-detected COs. The basic ideas were:

- to identify, for each CO detected in the closest SEVIRI time slot, the AMSU FOVs affected by convection and use the corresponding AMSU precipitation rates to calculate the mean precipitation associate to the CO and
- to apply a rigid shift to AMSU-derived precipitation of ± 3 FOVs in every directions and select the one which maximizes the amount of precipitation for each individual CO;

The estimated mean co-precipitation (MCP), Φ, was then computed as follows:

$$\Phi = \frac{\sum_{i=1}^{N} \mathrm{RR}_i * A_i}{\sum_{j=1}^{M} a_j},$$

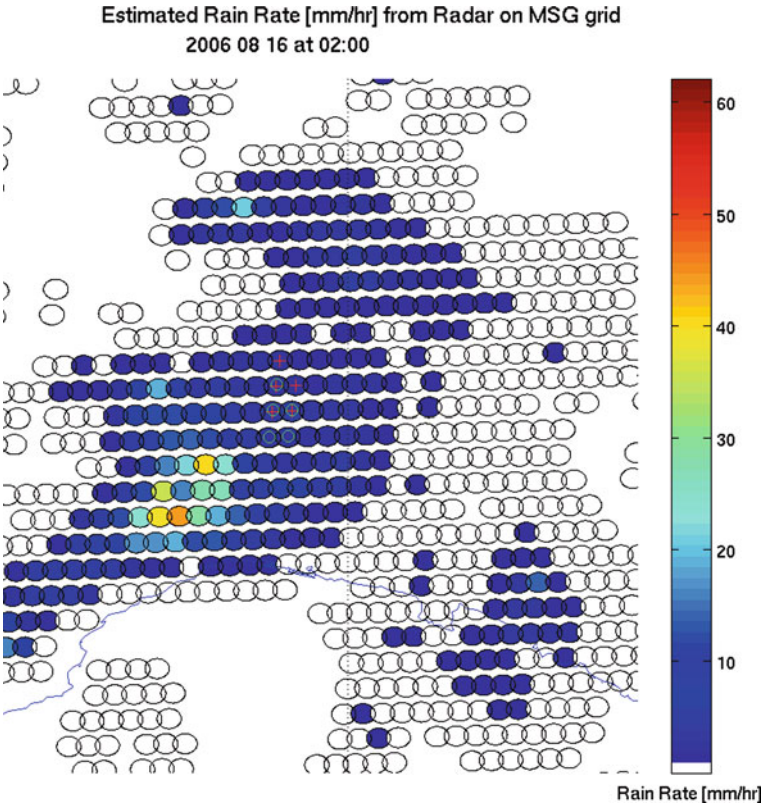

Fig. II.7.24 Parallax correction: the *colored circles* represent radar data interpolated and reprojected on the fixed SEVIRI grid, the *red crosses* are SEVIRI FOV characterized by convection before parallax correction, and the *green circles* are the same SEVIRI FOVs after parallax correction (For color figure see online version)

where RR_i is the AMSU-derived RR for the *j*th; A_i the area of the *i*th AMSU FOV; *i* goes from 1 to *N* with *N* being the number of AMSU FOVs affected by the convective object; a_j the area of the *j*th SEVIRI FOV; and *j* goes from 1 to *M*, with *M* being the number of SEVIRI FOVs within the convective object.

In summary, Φ represents the precipitation that would characterize the CO if all the precipitation observed in the corresponding AMSU FOVs was confined to the convective region only. This assumption represents an approximation, and it is intended to provide an upper bound to the precipitation associated to the CO. In its current implementation the algorithm calculates the AMSU IFOVs according to Bennartz (2000) and it accounts for the parallax error on the SEVIRI FOVs (Sect. 4.5.1), it also corrects for AMSU geolocation errors (Sect. 3.6.1) using a rigid shift scheme as previously described. In addition to the mean precipitation the algorithm generates also RR values for each SEVIRI pixel, identified as convective by nefodina, according to the following expression:

$$\phi_{i,j} = \frac{\mathrm{RR}_{i,j} * A_{i,j}}{\sum_{k=1}^{L} a_k},$$

where $\mathrm{RR}_{i,j}$ is the RR for the AMSU FOV in the ith row and jth column of the satellite swath; $A_{i,j}$ the area of the AMSU FOV in the ith row and jth column of the satellite swath; and a_k is the area of the kth SEVIRI convective FOV within the AMSU $A_{i,j}$ FOV, with k going from 1 to the total number of convective pixels, L, within the AMSU FOV.

The single pixel estimate ϕ is in general prone to geolocation and co-location errors. If fact if, due to a small geolocation error, a single SEVIRI pixel belonging to a broad CO which densely populate an AMSU FOV was erroneously located within a different AMSU FOV, its RR would have been much higher with respect to the average of the CO. Since even small errors in the AMSU geolocation can determine whether a SEVIRI FOVs belongs to one (less densely populated) or another (more densely populated) AMSU FOVs, this estimate might vary significantly within the same CO, and it is to be used in a careful way.

5.2 Product Description

The co-location products were differentiated into: MCP (Φ) values which define the mean RR for a nefodina CO; estimates ($\phi_{i,j}$) of RR for individual SEVIRI FOVs belonging to a nefodina CO. Since the first product, MCP, was more robust to geolocation and parallax errors, while the second product was generally prone to these errors and provided highly variable estimates even within the same CO, hereafter only results on MCP are discussed.

5.3 Qualitative Validation of Nefodina/AMSU Combined Products

Proper co-location of PC and nefodina had a central role in the development of the the MCP product. It represented the basis for merging geostationary and polar orbiting products which allowed for the identification of highly precipitating regions at SEVIRI spatial resolution (3–8 times finer than the native AMSU resolution), and under well-defined approximations it provided an upper bound estimates of the RR, within the convective regions. To describe the validation procedure established to evaluate MCP, the following example in Fig. II.7.25 is provided. The example shows the co-location of CO, as detected by nefodina, on the AMSU PC product. The selected data for this comparison were related to the NOAA-15 overpass on April 24, 2008 at 15:30 UTC. The figure shows the PC-weighted average for the AMSU along with different convective systems which were active in the scene (for sake of clarity only three systems over central Italy are shown to demonstrate the concept). The PC-weighted average RR for the AMSU overpass is represented by the color of the large FOVs, while the smaller SEVIRI FOVs indicate the location

Fig. II.7.25 PC-weighted average on AMSU native grid at 15:30 UTC and on SEVIRI FOVs

of the nefodina-detected COs. The COs co-locate nicely with the highly probable ($P \simeq 1$) class 4 (RR $>$ 5 mm/h) FOVs characterized by a weighted average RR of about 7 mm/h. Under the assumption that most of the precipitation occurred in the highly convective region, nefodina was shown to provide relevant information about the distribution of precipitation within the AMSU FOVs. Figure II.7.26 shows the same convective objects showed in Fig. II.7.25 but co-located with radar precipitation: the objects identified by nefodina properly matched the regions of highest radar precipitation, providing encouraging evidence that the hypothesis made on the precipitation distribution (highest where the convection is active) is solid. Quantitative comparisons for all the COs detected for this overpass and for the NOAA-16 overpass at 16:03 UTC are presented in Tables II.7.6 and II.7.7. The first raw of the tables

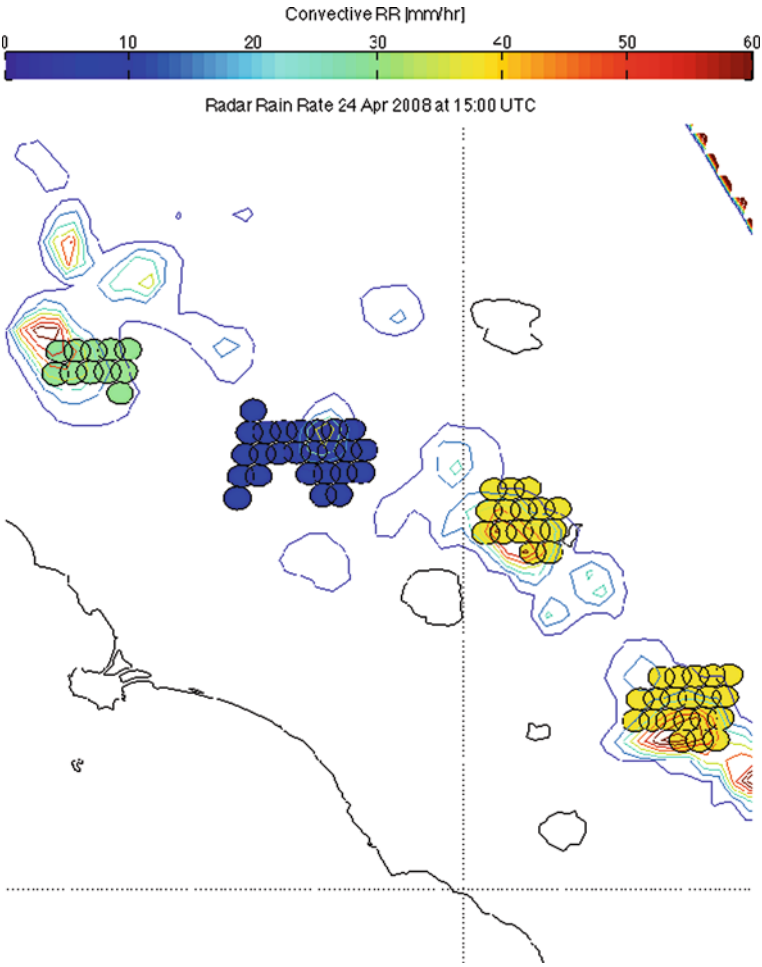

Fig. II.7.26 Radar RR compared to convective RR on SEVIRI grid 15:30 UTC (For color figure see online version)

Table II.7.6 Comparison of MCP and CO radar-derived convective RR for NOAA-15 overpass at 15:30 UTC

RR in mm/h	CO_1	CO_2	CO_3	CO_4	CO_5
RADAR 15:30 UTC	39	42	23	3	22
MCP 15:20 UTC	38	27	17	13	11

shows the radar RR averaged on the nefodina-detected COs, while the second raw shows the values of MCP for the same COs. The values of RR for MCP and radar exhibit a correlation $\rho = 0.66$ which, given the very limited size of the sample, is a purely indicative, but also encouraging, number.

Table II.7.7 Comparison of MCP and CO radar-derived convective RR for NOAA-16 overpass at 16:00 UTC

RR in mm/h	CO_1	CO_2	CO_3	CO_4
RADAR 16:00 UTC	27	25	21	16
MCP 15:55 UTC	36	41	46	18

6 Conclusions

This chapter described how in situ observations were used to show an important relation between the precipitation estimates derived by the PC algorithm at AMSU resolution and COs detected by nefodina at SEVIRI resolution. This relation opens the way to a potentially fruitful merging of geostationary and polar orbiting products which could improve the accuracy and the usefulness of the AMSU-derived precipitation products to hydrological and QPF activities. The case studies presented showed the good accordance between heavy rainfall (Class 4: RR > 5 mm/h) deduced by PC and convection detected by nefodina. They also showed encouraging results for the basic assumption on which the proposed merging strategy is based. For this study, the PC algorithm (Bennartz et al., 2002) developed within NWC-SAF was selected as the most suitable AMSU-based precipitation retrieval algorithm for the development of a convective precipitation product (MCP). The selection was based on pre-operational software availability, knowledge of performance characteristics over a large part of H-saf area (Northern Europe), use of AMSU channels more sensitive to heavy rainfall. The PC algorithm outputs were extended to the whole H-saf area allowing for testing and validation in the Mediterranean regions (Italy). Improvements in the performances of the algorithm were obtained through a refinement of the estimation of the radiative background field. AMSU data from NOAA 15, 16, 17, and 18 (and METOP after launch) were routinly processed, but lack of daily availability of radar data limited the validation activity. The precipitation observations from radar and rain gauges were collected only for a few Italian convective cases and upscaling and downscaling algorithms were developed to compare precipitation ground-based observations with PC algorithm retrievals and SEVIRI products. The validation procedure described in this chapter allowed:

- For improvements of the individual products. For the PC algorithm example, more than 43,000 RR retrievals taken in 7 different days from NOAA 16 and 18 data were compared to radar data convolved on the AMSU grid. The results obtained were on average 18%, with a peak of 58% for class 4, worse than those obtained by Bennartz (2005). This was explained by the fact that the background brightness temperature tuning that was originally developed for northern Europe frequently produces spurious rainfall signatures, especially in arid regions during daytime. On this basis a new approach for the estimation of the background BT in the PC algorithm was implemented to mitigate, and in most cases eliminate, the problem of spurious rainfall signatures.

- For tuning of a merging algorithm capable of taking into account geolocation and parallax errors which represented the most serious issues in combining SEVIRI-derived products with AMSU RRs.
- For verification that most of the precipitation does indeed occur in the detected convective portion of the cloud, hypothesis which represents the foundation of the MCP algorithm.
- For an initial evaluation of the MCP product with radar data.

Future work includes a more extensive validation with radar data and also a more accurate use of rain gauge data, only partially used in the described effort.

Appendix A Implementation Details on Data Projections

This appendix is included simply to clarify the methodology used for the inter-comparisons of the various products. In order to compare values derived at different resolutions, several procedures were implemented to remap products:

- from AMSU to SEVIRI grid;
- from radar to AMSU grid;
- from radar to SEVIRI grid;
- from gauges to SEVIRI grid.

In particular the SEVIRI grid was chosen as reference, since it provides a fixed grid at a convenient resolution.

A.1 The AMSU-to-SEVIRI Remapping Process

This process was designed to allow the comparison of current PC products with SEVIRI-derived rainfall products and with radar and rain gauge data on a fixed grid. However, it was also used to compute the background BTs for the PC algorithm (as described in Sect. 3.2). An example of the AMSU-SEVIRI remapping is shown in Fig. II.7.27.

The basic concepts of the implementation are hereafter described.

Given the location of a SEVIRI pixel, the bounds of the corresponding AMSU pixel are found. Routine begins by determining if it lies within the bounds of the AMSU grid, and if so, then searches for the closest AMSU observation. Having found the nearest AMSU, the routine then looks to the left and right (on the same AMSU row) to find which of these two is closer to the SEVIRI, and then the closest and its neighbor to the left or right are chosen as two of the four AMSUs surrounding the SEVIRI pixel. A check is performed to make sure the selected pixel is not on the lateral edge of the AMSU array, so that it makes sense to look left or right. If the pixel is on the edge, then the algorithm simply uses the two points on the row

nearest the edge. A weight is assigned to these two based on their distance from the SEVIRI pixel. The distances are determined by computing the angle between the SEVIRI position vector and either of the two chosen AMSU position vectors. This part of the algorithm, using vector algebra, is quite efficient.

Once the distances are calculated there are two different strategies to derive the BT on the SEVIRI grid. The first one makes simply use of the nearest neighbors, while the second interpolates (weighted average) among the four closest AMSU FOVs according to the following procedure: returning to the previously found nearest AMSU, the routine looks at the two AMSU points above and below, in adjacent rows, to find which of these two is closer to the SEVIRI point. The chosen row (above or below the row in which the closest AMSU lies) is then used, and the four points used for interpolation are the two found in the first row, and the two in the next-best row.

An interpolated estimated is made in each row (W_i) between the two chosen points on that row, using weights

$$\begin{aligned} W_{i1} &= 1 - s_1/(s_1 + s_2) \\ W_{i2} &= 1 - W_{i1} \end{aligned} \tag{3}$$

where s_1 and s_2 are the distances (in latitude degrees) between SEVIRI and the first and second closest AMSU points on that row. In the above case, if $s_1 = 0$ (i.e., an AMSU coincides with SEVIRI), then that AMSU has weight 1 and its neighbor has weight 0. A similar weighting scheme is then used vertically (W_j) along the AMSU column containing the closest AMSU to arrive at the weights which are used to interpolate as many of the AMSU channels as are needed to the SEVIRI location.

$$\begin{aligned} W_{j1} &= 1 - d_1/(d_1 + d_2) \\ W_{j2} &= 1 - W_{j1} \end{aligned} \tag{4}$$

where d_1 and d_2 are distances of two AMSUs along the minimal column from SEVIRI.

The horizontal weights and the vertical weights are then used to average the AMSU BTs (or any other quantity defined on the AMSU grid) on the two rows (e_1 and e_2):

$$\begin{aligned} e_1 &= W_{i1} * \mathrm{BT}(1,1) + W_{i2} * \mathrm{BT}(2,1) \\ e_2 &= W_{i1} * \mathrm{BT}(1,2) + W_{i2} * \mathrm{BT}(2,2) \\ e &= W_{j1} * e_1 + W_{j2} * e_2 \end{aligned} \tag{5}$$

to get the final estimate e of the BT.

The co-location scheme based on the nearest neighbors was used for the derivation of background BTs (as described in Section 3.5), while the second one (based on weighted averages) was used for validation purposes.

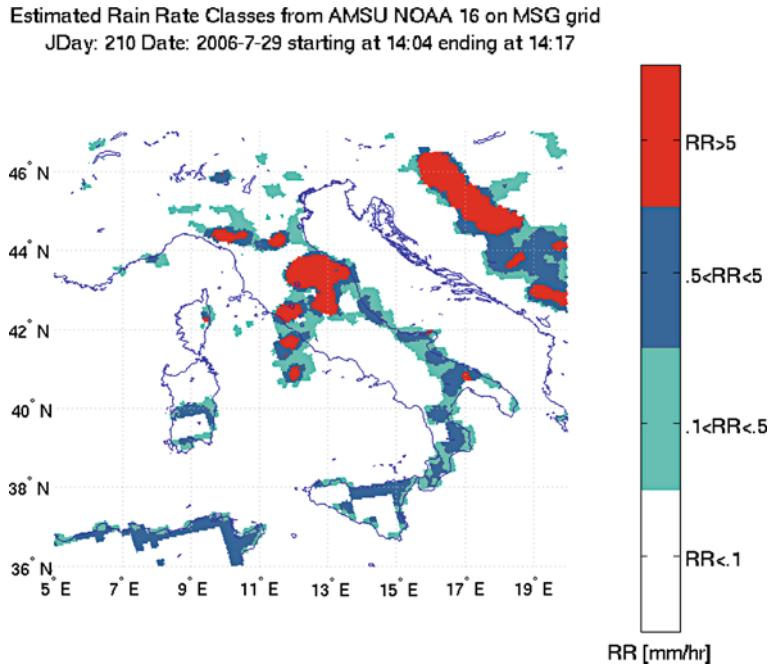

Fig. II.7.27 Example of PC remapping onto SEVIRI grid

A.2 The RADAR-to-AMSU Remapping Process

Radar data were convolved to the AMSU footprint using the methods described in Bennartz (1999), Bennartz and Michelson (2003), and Bennartz et al. (2002). The methods used in this study were initially derived for Baltex radar Data Center (BRDC) composites but were adjusted to account for the radar composites provided by CNMCA. The convolution takes into account the actual spatial sensitivity of AMSU-A and AMSU-B as outlined in Bennartz (2000). A fixed Z–R relation of $Z = 200R^{1.6}$ was used in this study. Due to missing information about the actual position of the radar in the composite imagery, a parallax correction could not be performed. Also, the radar data used in this study were not gauge adjusted.

A.3 The RADAR-to-SEVIRI Remapping Process

The observations available for surface rain intensity (SRI) were on a different scale (spatial resolution and projection) compared to satellite grids and since the variability of precipitation fields strongly depends on the scale at which the fields were considered a meaningful comparison was not trivial. The upscaling technique (fine to course resolution) used to remap radar data onto MSG grid, here described, is very

simple but numerically effective. National mosaic of SRI generated by radars and MSG product were composed of two static grids, each radar cell was linked to the SEVIRI pixel which contains the center of radar pixel. Therefore, radar data were remapped onto geostationary grid through the mean value of SRI calculated on radar cells linked to each satellite grid (Fig. II.7.28). An example of the RADAR-SEVIRI remapping is shown in Figs. II.7.29 and II.7.30.

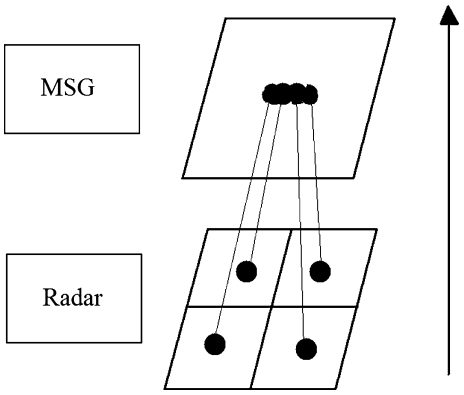

Fig. II.7.28 Radar-to-SEVIRI remapping scheme

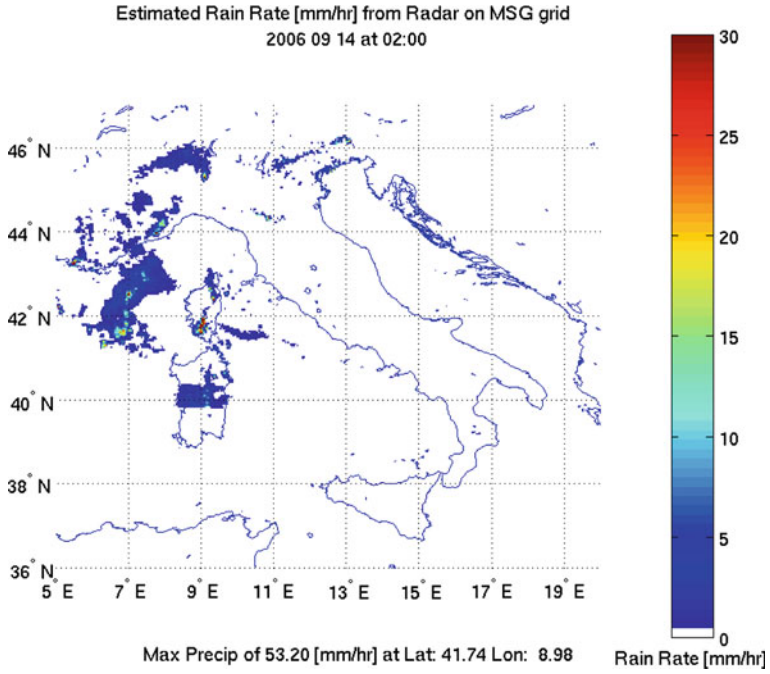

Fig. II.7.29 Example of radar-derived RR on SEVIRI grid

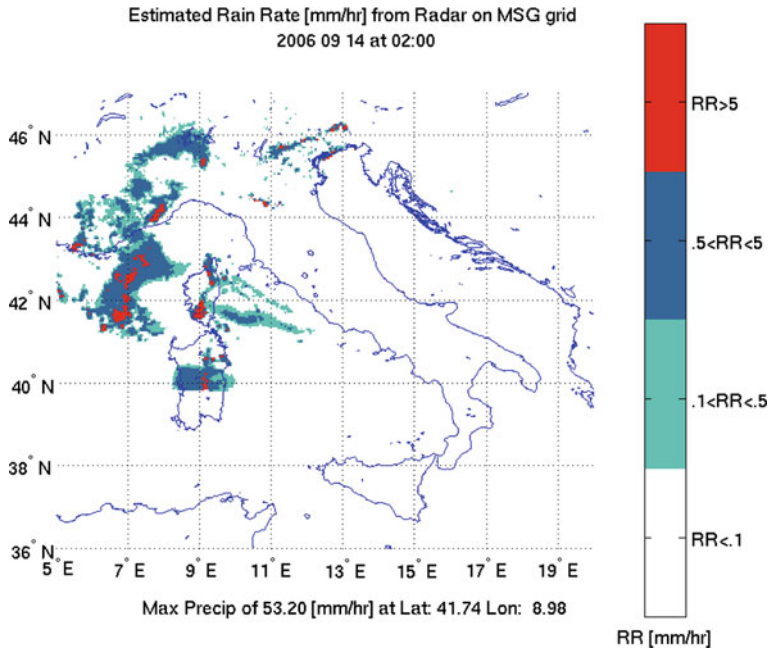

Fig. II.7.30 Example of radar-derived precipitation classes on SEVIRI grid

References

Bauer P (2001) Over-ocean rainfall retrieval from multisensor data of the tropical rainfall measuring mission. Part I: design and evaluation of inversion databases. J Atmos Ocean Technol 18(8):1315–1330

Bennartz R (1999) On the use of ssm/i measurements in coastal regions. J Atmos Ocean Technol 16:417–431

Bennartz R (2000) Optimal convolution of amsu-b to amsu-a. J Atmos Ocean Technol 17:1215–1225

Bennartz R (2005) Integration of Nowcasting SAF scattering indes into AAPP. EUMETSAT SAFNWC, Visiting Scientists Report, pp 1–4

Bennartz R, Michelson DB (2003) Correlation of precipitation estimates from spaceborne passive microwave sensors and weather radar imagery for baltex pidcap. Int J Remote Sens 24:723–739

Bennartz R, Thoss A, Dybbroe A, Michelson DB (2002) Precipitation analysis using the advanced microwave sounder unit in support of nowcasting applications. Meteorol Appl 9(2):177–189

Davenport JC, Vicente GA, Scofield RA (2007) The role of orographic and parallax corrections on real time high resolution rainfall rate distribution. Int J Remote Sens 23(2):221–230

Di Michele S, Mugnai A, Marzano FS, Poiares Baptista Tassa JPV (2003) A cloud model-based Bayesian technique for precipitation profile retrieval from the tropical rainfall measuring mission microwave imager. Radio Sci 38:8074

Grody NC, Zhao L, Meng H, Kongoli C, Pellegrino P, Qiu S, Ferraro RR, Weng F, Dean C (2004) Noaa operational hydrological products derived from the advanced microwave sounding unit (AMSU). IEEE Trans Geosci Remote Sens 43(5):1036–1049

Hong Y, Hafermann J, Olson WS, Kummerow C (2000). Microwave brightness temperatures from tilted convective systems. J Appl Meteorol 39:983–998

Kummerow C (1998) Beam-filling errors in passive microwave rainfall retrievals. J Appl Meteorol 37:356–370

Kummerow C, Giglio L (1994) A passive microwave technique for estimating rainfall and vertical structure information from space, part I: algorithm description. J Appl Meteorol 33(3):18

Panegrossi G, Dietrich S, Marzano FS, Mugnai A, Smith EA, Xiang X, Tripoli GJ, Wang PK, Poiares Baptista JPV (1998) Use of cloud model microphysics for passive microwave-based precipitation retrieval: significance of consistancy between model and measurement manifolds. J Atmos Sci 54:1644, 1673

Puca S, Biron D, De Leonibus L, Rosci P, Zauli F (2005) Improvements on numerical "objects" detection and nowcasting of convective cell with the use of seviri data (ir and wv channels) and numerical techniques. In: The international symposium on nowcasting and very short range forecasting (WSN05)

Puca S, Zauli F, De Leonibus L, Rosci P, Antonelli P (2009) Automatic detection and monitoring of convective cloud systems based on geostationary infrared observations. Meteorol Appl (Submitted)

Wolf R (1999) Lrit/hrit global specification coordination group for meteorological satellites. Technical Report 2.6. EUMETSAT, August 1999